

Elastic Neutron Scattering Measurements Using Larmor Precession of Polarized Neutrons

M.Th. Rekveldt¹, W.G. Bouwman¹, W.H. Kraan¹, O. Uca¹, S.V. Grigoriev¹,
K. Habicht², and T. Keller³

¹ Interfacultair Reactor Instituut, Delft University of Technology,
Mekelweg 15 2629 JB Delft, The Netherlands

² BENSC, Hahn Meitner Institut,
Glienicke Strasse 100 D-14109 Berlin, Germany

³ Max-Planck-Institute for Solid State Research,
Heisenbergstr. 1, D-70569 Stuttgart, Germany

Abstract. An overview will be given of new instruments using Larmor precession of polarized neutrons in precession regions with inclined front and end faces. These instruments concern small angle scattering, neutron reflectometry and high-resolution diffraction. The advantages of the first application, spin echo small angle scattering (SESANS), with respect to conventional SANS, is the range of applicability and orders of magnitude higher available intensity. The reflectometry application makes it possible to measure the momentum dependent intensity without hindrance of the waviness of the sample also with the high intensity of SESANS. The high resolution application enables one to measure very high resolution diffraction (10^{-5} relative in momentum space) without angular or wavelength confinement of the beam, thus with very high intensity.

Introduction

The instruments discussed in this paper are based on Larmor precession of polarized neutrons. The precession angle φ goes proportional to the magnetic field B and the interaction time with that field and thus with the wavelength λ and the length L of the path through this field:

$$\varphi = c\lambda BL \quad (1)$$

in which c is a constant determined by the magnetic moment of the neutrons ($c = 4.6368 \cdot 10^{14} \text{ T}^{-1} \text{ m}^{-2}$). Until recently the precession has been used to analyze only the wavelength or the magnetic field and interaction time with that field. The application of the first is the well-known spin echo technique introduced by Mezei [1], who used the echo of two precession regions to determine very precisely the wavelength change and thus the energy transfer in a sample. The application of the second is the well-known neutron depolarization technique [2,3,4,5].

In this paper Larmor precession will be considered to encode not only the wavelength of a neutron beam, but to encode also the transmission angle through the precession device. The latter is possible if inclined front and end faces of the precession devices are used. The idea to encode the direction of the neutron

trajectory was considered a long time ago by Pynn [6] for focussing purposes in neutron spin echo and line width studies in elastic diffraction . It received interest again in the demonstration of the new resonance spin echo technique by Keller *et al.* [5]. We recently considered inclined front and end faces of the precession devices in more detail [8]. We demonstrated that it is possible to encode the angle of transmission through the device for various purposes. Together with the wavelength encoding this opens up, besides the normal spin echo applications, applications in SANS [9,10], neutron reflectometry [11] and high-resolution neutron diffraction [12,13].

1 Angle and/or Wavelength Encoding with Larmor Precession

The principle of encoding the angle of transmission through the precession device is sketched in Fig. 1, where the front and end faces of the precession device make an angle of θ_0 with its main axis. The latter coincides with the average transmission direction of the neutron beam. The intensity after transmission through this setup is determined by the precession angle φ of the polarization in the precession device. It can be written as,

$$I(\varphi) = I_s(1 + P_0 \cos(\varphi)) \quad (2)$$

with I_s the so-called shim intensity of the fully depolarized beam and

$$\varphi = c\lambda BL \frac{\sin \theta_0}{\sin(\theta_0 + \theta)} = c\lambda BL(1 + \theta \cot \theta_0 + O(\theta^2)) \quad (3)$$

where θ is the angular deviation of a certain neutron path from the main axis, B the magnetic field in the precession device, and L its length measured along the main axis (see Fig. 1). Eq. 3 shows that the precession angle φ encodes the wavelength as well as the transmission angle θ .

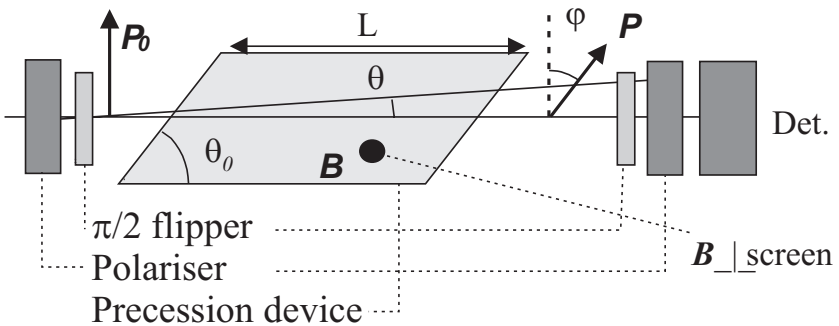


Fig. 1. Setup consisting of a polarizer P , a $\pi/2$ flipper to orient the polarization perpendicular to the field B in the precession device, a precession device, a second $\pi/2$ flipper, a second polarizer and a detector. The inclined front and end face cause a different precession angle with different transmission angle θ through the device. We call this property “encoding of transmission angle”.

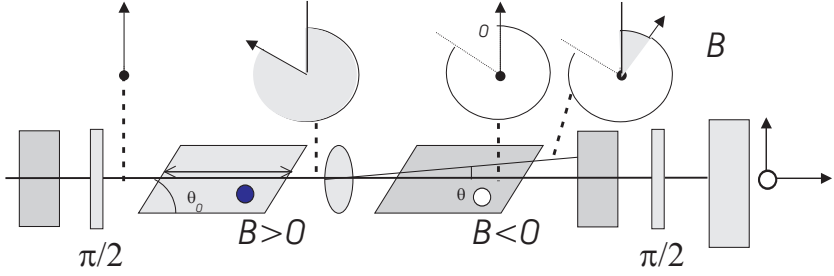


Fig. 2. The spin echo setup consists of two precession devices with opposite magnetic fields, that cancel the precession angles of the passing neutron spins, when nothing occurs to the neutrons during transmission. When the transmission direction changes in a sample between the two devices the net precession angle changes. In the top of the figure the rotations along different paths are indicated.

1.1 Spin Echo Small Angle Neutron Scattering (SESANS)

Two of such identical devices in series with opposite magnetic fields create a spin echo setup that enables one to measure small angle scattering of a sample positioned just between the precession devices. A sketch of the setup is given in Fig. 2. The technique works as follows. After polarizing the beam in the polarizer P , the polarization is rotated by a $\pi/2$ flipper to a direction perpendicular to the magnetic field direction of the precession devices. Entering the precession devices the polarization starts to precess around the field during the time of presence in that field. According to eq. 3 the net precession angle φ after passing the two precession regions with opposite magnetic fields and different transmission angles θ_1 and θ_2 is given by,

$$\varphi = \varphi_2 - \varphi_1 = c\lambda BL \cot \theta_0 (\theta_2 - \theta_1) \equiv zQ_z \quad (4)$$

with

$$z = \frac{c\lambda^2 BL \cot \theta_0}{2\pi} \quad (5)$$

Here the angle difference $(\theta_2 - \theta_1)$ has been translated to a momentum transfer Q_z by some scatterer between the precession devices. The complementary quantity z of Q_z defines a length that we will call the spin echo length, in analogy with the spin echo time. This length can be scanned by varying the quantities λ , B , L or θ_0 . The polarization after the two devices is analyzed by a second $\pi/2$ rotator and polarization analyzer.

Single scattering. In terms of the spin echo length z eq. 2 can be rewritten as:

$$I(z) = I_s(1 - P(z)) \quad (6)$$

with

$$P(z) = 1 - \sigma t + \sigma G(z)t \quad (7)$$

and

$$\sigma = \frac{1}{k_0^2} \int dQ_y dQ_z d\sigma/d\Omega(\mathbf{Q}) \quad (8)$$

$$G(z) = \frac{1}{\sigma k_0^2} \int dQ_y dQ_z d\sigma/d\Omega(\mathbf{Q}) \cos(Q_z z) \quad (9)$$

Here k_0 is the momentum of the incident beam, σt represents the fraction of the polarized beam that scatters in the sample of thickness t with momentum transfer vector $\mathbf{Q} = Q_y \mathbf{e}_y + Q_z \mathbf{e}_z$ and differential cross-section $d\sigma/d\Omega(Q)$. The quantity σ is the total scattering cross-section, hence $1 - \sigma t$ is the fraction of un-scattered neutrons that did not change their transmission direction and as a consequence did not change polarization. The product $G(z)t$ refers to the fraction of the beam that scattered and therefore changed its polarization according to eq. 9.

Correlation function $G(z)$. One may note that $G(z)$ is a kind of Fourier transform of $d\sigma/d\Omega(Q)$. From eq. 7 and eq. 9 follows that the measured polarization change as a function of the spin echo length z yields directly this correlation function $G(z)$ of the scattering inhomogeneity of the sample. This correlation function is in real space and therefore directly related to the structure of the sample studied. Calculations show that the spin echo length at which the polarization saturates corresponds to the longest length scale in a dilute system [10]. Calculations of $G(z)$ for spherical concentric multi shell particles show that the number of peaks in the polarization corresponds to the number of shells in such a system [9]. The location of the peaks corresponds also to the radii of the shells. It seems to be closely related to the distance probability function, denoted $\gamma(r)$ by Glatter [14].

Multiple scattering. In case that multiple scattering is present the formulae are somewhat more complicated and eq. 7 should be written as

$$P(z) = 1 - s_t + G'(z, t) \quad (10)$$

with s_t the scattered fraction by the sample and $G'(z, t)$ representing the fraction of the beam modified in polarization by the changed transmission angle. The scattering in the sample can be thought to be built up of the scattering processes taking place along an individual path. Let us assume that n scattering events happen, with the probability for one such event equal to ρ_n . The chance is given by [15]:

$$\begin{aligned} \rho_n &= \frac{t^n \int dQ_{1y} dQ_{1z} \frac{d\sigma}{d\Omega}(Q_1) \int dQ_{2y} dQ_{2z} \frac{d\sigma}{d\Omega}(Q_2) \dots \int dQ_{ny} dQ_{nz} \frac{d\sigma}{d\Omega}(Q_n)}{k_0^{2n} 1 \times 2 \times \dots \times n} T \\ &= \frac{(\sigma t)^n}{n!} T \end{aligned} \quad (11)$$

with

$$Q_1 + Q_2 + \dots + Q_n = Q \quad (12)$$

and T is the transmission of un-scattered neutrons given by

$$T \equiv 1 - s_t. \quad (13)$$

The total scattering is found by summing over all path probabilities ρ_n

$$s_t = \sum_{n=1}^{\infty} \rho_n = \sum_{n=1}^{\infty} \frac{(\sigma t)^n}{n!} T = T(e^{\sigma t} - 1) = 1 - e^{-\sigma t} \quad (14)$$

and thus $T = \exp(-\sigma t)$. Let us now evaluate the second term $G'(z, t)$ on the right hand side of eq. 10. The total wave vector transfer Q_z in the cosine term of this equation is the sum of all individual transfers according eq. 12 occurring during the passage in one path through the sample and in particular the cosine term $\cos(Q_z)$ can be written as

$$\cos(Q_z) = \cos(Q_{1z}) \cos(Q_{2z}) \dots \cos(Q_{nz}) \quad (15)$$

+ odd terms in Q_1, Q_2 and Q_n . In the integrals over Q_i the odd terms in Q_i do not contribute and can be omitted. In a similar way as done for the total scattering derivation in eq. 11 to eq. 14 we find

$$\begin{aligned} \rho'_n &= \frac{t^n \int dQ_{1y} dQ_{1z} \frac{d\sigma}{d\Omega}(Q_1) \cos(Q_{1z}z)}{k_0^{2n} 1 \times 2 \times \dots \times n} \\ &\quad \times \int dQ_{2y} dQ_{2z} \frac{d\sigma}{d\Omega}(Q_2) \cos(Q_{2z}z) \\ &\quad \times \dots \int dQ_{ny} dQ_{nz} \frac{d\sigma}{d\Omega}(Q_n) \cos(Q_{nz}z) \times T \\ &= \frac{(\sigma G(z)t)^n}{n!} T \end{aligned} \quad (16)$$

and

$$G'(z, t) = \sum_n \rho'_n = \sum_{n=1}^{\infty} \frac{(\sigma G(z)t)^n}{n!} T = T(e^{\sigma G(z)t} - 1) \quad (17)$$

Substituting this result in eq. 10 we find for $P(z)$ in case of multiple scattering:

$$P(z) = T + G'(z, t) = T e^{\sigma G(z)t} = e^{\sigma t(G(z)-1)} = T^{1-G(z)} \quad (18)$$

or

$$G(z) = 1 - \frac{\ln(P(z))}{\ln(T)} \quad (19)$$

This equation shows that there is a one-to-one relation between the measured polarization and the correlation function $G(z)$ independent of possible multiple scattering, provided the level s_t or T can be defined. That means that one does not need to limit the number of scattering processes of the neutrons in transmission through the sample, contrary to conventional SANS where the sample thickness must be chosen such as to avoid multiple scattering. This is a great advantage of the SESANS technique in view of measuring statistics.

If one does not know the transmission or the total amount of scattering, it is still possible to scale the depolarization with the thickness to obtain the shape of the correlation function:

$$\frac{\ln(P(z))}{t} = \sigma(G(z) - 1). \quad (20)$$

1.2 Neutron Reflectometry

For reflectometry two different setups can be built with different properties. First, by using the two devices in the geometry as discussed in the previous section [8,11], the precession devices with inclined faces can also be used to study the momentum dependent intensity in neutron reflectometry. The formulae derived for SESANS in single scattering in eq. 4 and eq. 7 can be formulated as

$$\varphi_1 - \varphi_2 = zQ \quad (21)$$

and

$$I(z) = I_s(q_1) \int dQ_z R(Q_z)(1 + \cos(zQ_z)) \quad (22)$$

where $I_s(q_1)$ is the incident depolarized intensity that is weakly dependent on the incident wave vector q_1 . Like in the case of SESANS, the measured intensity $I(z)$ is just the Fourier transform of the scattering cross-section as a function of momentum transfer Q . In reflectometry the latter is the reflectivity function $R(Q_z)$. The most surprising result is that now $R(Q_z)$ is measured independent of possible waviness of the sample and without any confinement of the incident beam. Because in general this $R(Q_z)$ is a strongly changing function of Q_z , the use of this technique is recommended in combination with a position dependent detector or a low resolution time of flight monochromatisation to make already a rough distinction in Q_z regions, in order to circumvent the disadvantages of the Fourier techniques, that makes them less sensitive for low intensity features in the measured spectrum. When this option is used far enough away from total reflection, the local structure perpendicular to the surface is directly probed by $I(z)$ by the spin echo length z .

Let us now consider the second case that we configure the set-up with a mirror plane between the precession regions, see Fig. 3. In this case all arguments used in SESANS can be used in this reflection geometry. Specular reflection will lead to a zero net precession angle, while off-specular reflection will change this angle and lead to depolarization of the beam. In formula

$$\varphi_1 - \varphi_2 = cB\lambda \cot \theta_{01}(\psi_1 - \psi_2) \quad (23)$$

and

$$I(B) = I(\psi_1) \int dx R(x)(1 + \cos(cB\lambda \cot \theta_{01}(\psi_1 - \psi_2))) \quad (24)$$

From these equations it appears possible to separate the specular and off-specular reflection by only two measurements at zero and high magnetic field in the precession devices. The depolarization measured at high field gives immediately the

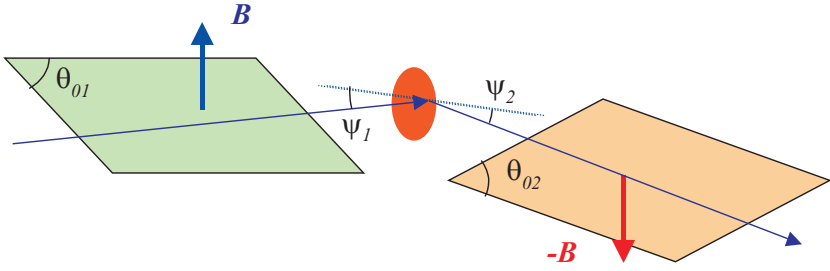


Fig. 3. Schematic diagram of the second reflectometer mode. The set-up is in principle the same as the SESANS setup, with only a mirror plane introduced between the precession regions. This opens new applications especially in neutron reflectometry as explained in the text.

fraction of off-specular reflected neutrons. More extensive measurements over the whole B range yield like in the SESANS case, the full correlation function of the inhomogeneities leading to the off-specular reflection. Especially this correlation function can be measured parallel and perpendicular to the reflection plane of the sample, by rotation of the precession devices with respect to the reflection plane.

1.3 High-Resolution Larmor Diffraction

Two of such devices in series with parallel magnetic fields and the inclination angles matched in such a way that the precession regions form a precession region according to Fig. 4, create a very powerful diffraction instrument. This can be explained in two different ways. In a geometrical way one can see that the path lengths of the incoming and outgoing neutron in Fig. 4 have lengths L_1 and L_2 , given by

$$L_1 = L / \sin(\theta_b + \varepsilon) \quad \text{and} \quad L_2 = L / \sin(\theta_b - \varepsilon) \quad (25)$$

in which θ_b is the scattering angle and ε a mismatch between the reflecting plane with respect to the inclination angle of the precession device. Realising further that the wave vector component perpendicular to the precession face is given by:

$$k_{1\perp} = \frac{2\pi \sin(\theta_b + \varepsilon)}{\lambda} \quad \text{and} \quad k_{2\perp} = \frac{2\pi \sin(\theta_b - \varepsilon)}{\lambda} \quad (26)$$

which combines to the precession angle

$$\varphi = c\lambda B(L_1 + L_2) = 2\pi cBL \left(\frac{1}{k_{1\perp}} + \frac{1}{k_{2\perp}} \right). \quad (27)$$

This equation can be understood if one realizes that the precession angle depends on the time spent in a magnetic field, so it is inversely proportional to the component of the velocity (hence momentum transfer) perpendicular to the

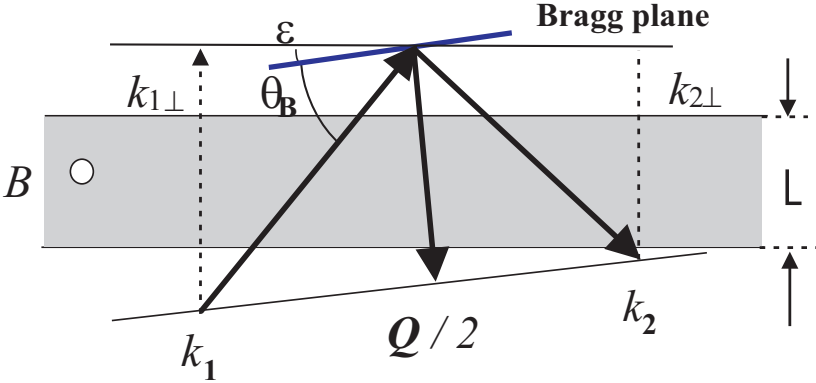


Fig. 4. Sketch of the high-resolution Larmor precession device. The travel time of the neutrons through the device matches just the momentum transfer component Q_{\perp} that makes that the spread in precession angles of the polarization yield directly the spread in Q_{\perp} , independent of angular and wavelength spread of the incident beam.

device. The total travel time through the precession device is given by the sum of the inverses of the perpendicular component of the incident and final wave vector k_1 and k_2 . Thus the precession angle of the neutron beam incident and reflected can be calculated with some geometry

$$\varphi = 2\pi cBL \frac{k_{1\perp} + k_{2\perp}}{k_{1\perp}k_{2\perp}} = \varphi_0(1 + \cot^2 \theta_B \tan^2 \varepsilon) \quad (28)$$

with

$$\varphi_0 = \frac{8\pi cBL}{Q_{\perp}} \quad (29)$$

and the measured modulation term $\cos(\varphi)$ can be calculated by averaging over ε . Because ε appears in eq. 28 quadratically, this averaging will deliver a damping $A_0(\varphi_0)$ and also a little phase shift c'' as defined in the next formula

$$\langle \cos(\varphi) \rangle \equiv A_0(\varphi_0) \cos((\varphi_0(1 + c''))). \quad (30)$$

The amplitude and phase shift follow from the next evaluation,

$$\langle \cos(\varphi) \rangle = \frac{1}{X} \int dx \cos(\varphi_0(1 + x^2)) \quad (31)$$

with $x = \varepsilon \cot \theta$ and $X = \varepsilon_0 \cot \theta$.

$$\begin{aligned} \langle \cos(\varphi) \rangle &= \frac{1}{X} \int dx (\cos \varphi_0 \cos(\varphi_0 x^2) - \sin \varphi_0 \sin(\varphi_0 x^2)) \\ &\approx \frac{1}{X} \int dx (1 - \frac{\varphi_0^2 x^4}{2}) \cos(\varphi_0) - \varphi_0 x^2 \sin \varphi_0 \\ &= (1 - \frac{\varphi_0^2 X^4}{10}) \cos(\varphi_0) - \varphi_0 \frac{X^2}{3} \sin \varphi_0 \end{aligned} \quad (32)$$

$$\approx \sqrt{1 - \frac{\varphi_0^2 X^4}{5} + \frac{\varphi_0^2 X^4}{9}} \cos(\varphi_0(1 + \frac{X^2}{3})).$$

This results for $A_0(\varphi_0)$ and c''

$$A_0(\varphi_0) = \left(1 - \frac{4}{90} (\varphi_0)^2 \varepsilon_0^2 \cot^4 \theta_B\right) \quad \text{and} \quad c'' = \frac{1}{3} \varepsilon_0^2 \cot^2 \theta_B \quad (33)$$

The amplitude $A_0(\varphi_0)$ is a damping factor only weakly dependent on the mismatch ε_0 of the reflecting plane with respect to the inclination angle of the precession device. In the derivaton of $A_0(\varphi_0)$ we have for convenience assumed a rectangular distribution of ε with total width $2\varepsilon_0$. The amplitude itself can be considered as a kind of resolution function.

In a real diffraction pattern the resulting intensity can be described in a similar way as for the SESANS and the reflectometry. One measures a kind of Fourier transform of the scattered intensity $S(Q)$:

$$I(B) = I_0 \left(1 + \int dQ_{\perp} S(Q_{\perp}) A_0(\varphi_0) \cos(\varphi_0)\right) \quad (34)$$

In the above equation we have omitted the small correction $(1+c'')$ in the phase φ_0 for convenience of writing. For a single Bragg peak with a finite width eq. 34 can be described as an extra damping $A(\varphi_0)$ due to the spread in Q_{\perp} values:

$$I(B) = I_0 (1 + A(\varphi_0) A_0(\varphi_0) \cos(\varphi_0)) \quad (35)$$

It appears that the extra damping is just the Fourier transform of the diffraction line profile $F(x)$ with $x = Q_0/Q_{\perp}$ and Q_0 the average wave vector of the diffraction line, according to the formula,

$$A(\varphi_0) = \frac{1}{N} \int dx F(x) \cos(\varphi_0 x). \quad (36)$$

Phase changes of $\Delta Q/Q = 10^{-6}$ and line widths of $\Delta Q/Q = 10^{-4}$ to 10^{-5} are measurable.

2 SESANS

Single scattering. In Fig. 5 the depolarization due to small angle scattering of a concentrated solution of polystyrene spheres with a diameter of 200 nm is shown. The depolarization saturates at a spin echo length $z = 100$ nm at a polarization of 0.9. The length scale corresponds roughly with the diameter, it does not match exactly, which could be due to the interference between the particles which manifests itself in the structure factor. The saturation level indicates a total scattering of 10 %, which agrees with the calculated amount of scattering from the scattering length contrast between the polystyrene and the H_2O . Lebedev *et al.* [16] obtained similar results with scattering of latex particles, using gratings to create a modulation in the scattering angle. We will do conventional SANS measurements on the same sample as a calibration of these measurements.

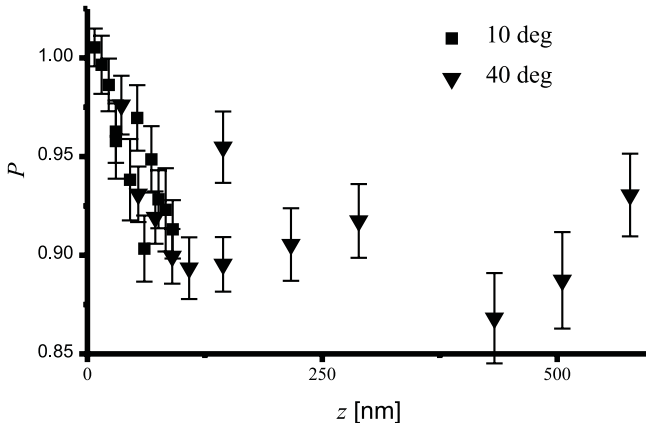


Fig. 5. SESANS signal of polystyrene spheres with a diameter of 200 nm with a volume concentration of 0.1 dissolved in H₂O. The measurements were performed at the Hahn-Meitner-Institut, Berlin with the neutron resonance spin echo setup. A wavelength of $\lambda = 5.827 \text{ \AA}$ was used. The tilt angle of the coils was set at 10° (squares) and 40° (triangles) to vary the sensitivity range of the set-up. The data are normalised to the polarization of the empty beam.

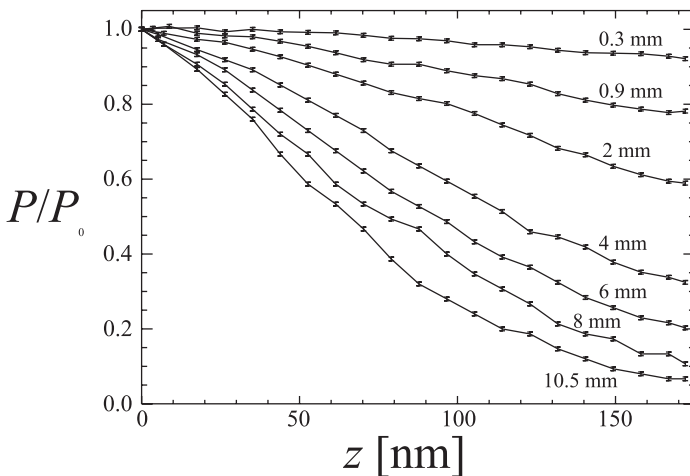


Fig. 6. SESANS signal of several thicknesses of limestone powder. The measurements are performed at IRI, Delft with a magnetised foil setup. A wavelength of $\lambda = 2.05 \text{ \AA}$ is used. The signal is due to the surface structure of the powder particles or due to double Bragg scattering.

Multiple scattering. Multiple scattering results in peak broadening in conventional SANS. In SESANS it results therefore in stronger decay of the polarization as a function of z as one can see in Fig. 6. Not only the amount of depolarization changes, but also the shape becomes narrower for thicker samples. Scaling the polarization according to eq. 20 gives a collapse of all data on one single curve

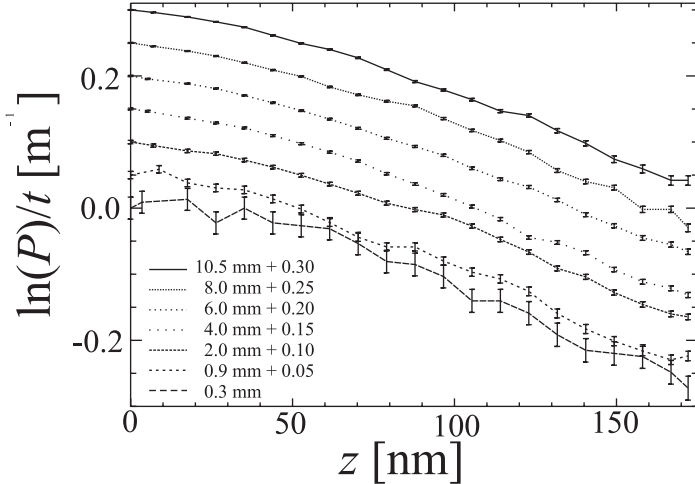


Fig. 7. Data in Fig. 6 scaled according to eq. 20 with the thickness to obtain the shape of the correlation function $G(z)$. The curves collapse on one single curve when they are plotted on the same scale. Only the counting statistics are taken into account in the error bars. To illuminate the differences in the error bars curves have each been shifted in scale by 0.05 mm^{-1} with respect to each other.

which is directly proportional to the correlation function $G(z)$ as shown in Fig. 7. The error bars in the scaled measurements are the lowest in each spin echo length region for different thicknesses. The relative errors in the polarization are the smallest when the polarization is far away from 0 and 1. The error bars in the scaled polarization are therefore smallest for short spin echo length z for thick samples and for long spin echo length z for thin samples. This makes it possible to vary the sensitivity range of the experiment by varying the thickness.

3 High Resolution Larmor Diffraction

Measurements have been carried out using the zero-field spin echo setup at HMI in Berlin [5], using the setup not in spin echo mode but switching the second precession arm in parallel mode. The first experiment to show that the technique works was measuring the (111) reflection of perfect silicon wafers under varying bending stress. As the stress increased the elastic deformation in the wafers increases, too. This leads to a variation in lattice spacing under reflection and hence to a damping of the Larmor precession amplitude with increasing precession angle φ_0 . Fig. 8 shows the damping as function of the precession angle of the (111) reflection of 0.5 mm thick silicon wafers in various bending states as indicated in the figure by the radius of curvature R . Other examples of diffraction are given in [13].

Because of the great sensitivity, this high-resolution diffraction method may be used effectively in structure determination, distribution of crystallites in powders in the spatial range of microns, stress distributions in deformed materials

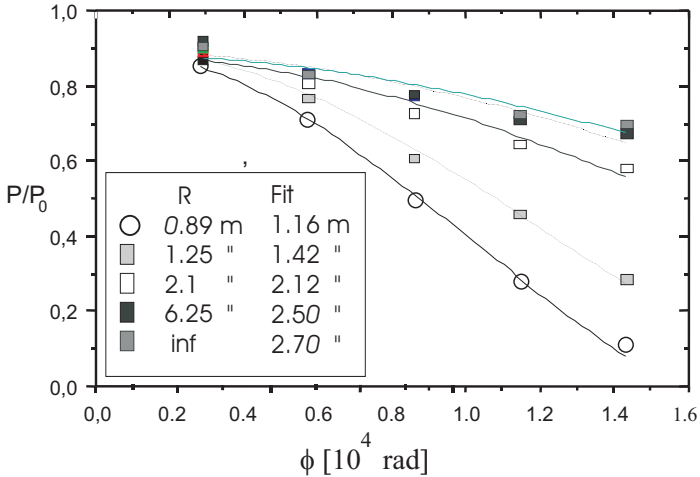


Fig. 8. Damping of the precession amplitude from the (111) reflection of 0.5 mm thick silicon wafers as a function of the precession angle at different bending states of the silicon wafers. The bending is indicated in the figure by the radius of curvature R .

and diffraction line broadening. Local strains of 10^{-4} to 10^{-5} are measurable, while relative lattice spacing changes down to 10^{-6} are measurable.

Conclusions

Techniques using Larmor precession can overcome several limitations existing in conventional diffraction techniques. It appears possible to identify the Larmor precession angle directly in a single diffraction parameter as momentum transfer or energy transfer, which makes the Larmor technique independent of diffraction parameters like wavelength and angular resolution. This has great consequences for usable intensity in the experiments. Where in conventional diffraction the incident and final angular and wavelength resolution are the limiting factors in available intensity and achievable resolution, in the Larmor technique these limitations are absent. The achievable accuracy is only limited by the quality of the precession device that limits the total precession angle achievable. In the SESANS option inhomogeneities up to the micron region are measurable, while in the high resolution diffraction mode line spacing variations of 10^{-6} and line widths of the order 10^{-5} can be determined. In the reflection mode the possibility of measurement of the momentum transfer without limitations of waviness of the sample should be mentioned. One disadvantage of the Larmor techniques should be mentioned. Small features in a specific measurement can be darkened by big features. For that purpose the use of a rough discrimination of wavelengths or angle, using a pulsed beam or position sensitive detector, respectively, may be advantageous.

Acknowledgement

This work is part of the research programme of the ‘Stichting voor Fundamenteel Onderzoek der Materie (FOM)’, which is financially supported by the ‘Nederlandse Organisatie voor Wetenschappelijk Onderzoek (NWO)’. We acknowledge the support of the European Community – Access to Research Infrastructure action of the Improving Human Potential Programme.

References

1. F. Mezei, *Neutron Spin Echo*, Lecture Notes in Physics, Vol. 128 (Springer Verlag, Berlin, 1980)
2. O. Halpern, T. Holstein, *Phys. Rev.* **59**, 960 (1941)
3. S.V. Maleev, V.A. Ruban, *Sov. Phys. JETP* **31**, 111 (1970)
4. M.Th. Rekveldt, *J. de Phys. Colloq. C1* **32**, 579 (1971)
5. M.Th. Rekveldt, *Z. Physik* **259**, 391 (1973)
6. R. Pynn, Neutron spin echo and three-axis spectrometers, in *Neutron Spin Echo*, Lecture Notes in Physics, Vol. 128, ed. by F. Mezei (Springer Verlag, Berlin, 1980) p. 159
7. T. Keller, R. Gähler, H. Kunze, R. Golub, *Neutron News* **6**, 16 (1995)
8. M.Th. Rekveldt, *Physica B* **276**, 55 (2000)
9. W.G. Bouwman, M.Th. Rekveldt, *Physica B* **276-278**, 126 (2000)
10. M.Th. Rekveldt, *Nucl. Instr. & Methods in Phys. Res. B* **114**, 366 (1996)
11. M.Th. Rekveldt, *Physica B* **234**, 1135 (1997)
12. M.Th. Rekveldt, *Materials Science Forum* **21-3**, 258 (2000)
13. M.Th. Rekveldt, W.H. Kraan, *J. Neutron Research* **8**, 53 (1999)
14. O. Glatter, *J. Appl. Cryst.* **12**, 166 (1979)
15. J. Schelten, W. Schmatz, *J. Appl. Cryst.* **13**, 385 (1980)
16. V.T. Lebedev, A.D. Dudakov, L. Cser, L. Rosta, Gy. Torok, *J. de Phys. Colloq. C8* **3**, 481 (1993)